

Bonding in Complexes of Bis(pentalene)dititanium, $Ti_2(C_8H_6)_2$

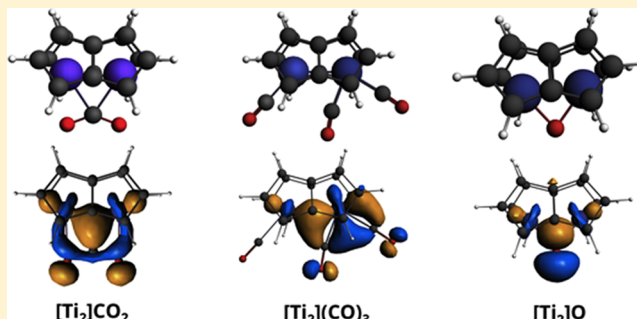
Alexander F. R. Kilpatrick,[†] Jennifer C. Green,^{*,‡} and F. Geoffrey N. Cloke^{*,†}

[†]Department of Chemistry, School of Life Sciences, University of Sussex, Brighton BN1 9QJ, U.K.

[‡]Department of Chemistry, University of Oxford, Inorganic Chemistry Laboratory, South Parks Road, Oxford OX1 3QR, U.K.

Supporting Information

ABSTRACT: Bonding in the bis(pentalene)dititanium “double-sandwich” species Ti_2Pn_2 ($Pn = C_8H_6$) and its interaction with other fragments have been investigated by density functional calculations and fragment analysis. Ti_2Pn_2 with C_{2v} symmetry has two metal–metal bonds and a low-lying metal-based empty orbital, all three frontier orbitals having a_1 symmetry. The latter may be regarded as being derived by symmetric combinations of the classic three frontier orbitals of two bent bis(cyclopentadienyl) metal fragments. Electrochemical studies on $Ti_2Pn_2^{+2}$ ($Pn^+ = 1,4\{-Si^iPr_3\}_2C_8H_4$) revealed a one-electron oxidation, and the formally mixed-valence $Ti(II)-Ti(III)$ cationic complex $[Ti_2Pn_2^{+2}][B(C_6F_5)_4]$ has been structurally characterized. Theory indicates an $S = \frac{1}{2}$ ground-state electronic configuration for the latter, which was confirmed by EPR spectroscopy and SQUID magnetometry. Carbon dioxide binds symmetrically to Ti_2Pn_2 , preserving the C_{2v} symmetry, as does carbon disulfide. The dominant interaction in $Ti_2Pn_2CO_2$ is σ donation into the LUMO of bent CO_2 , and donation from the O atoms to Ti_2Pn_2 is minimal, whereas in $Ti_2Pn_2CS_2$ there is significant interaction with the S atoms. The bridging O atom in the mono(oxo) species Ti_2Pn_2O , however, employs all three O 2p orbitals in binding and competes strongly with Pn , leading to weaker binding of the carbocyclic ligand, and the sulfur analogue Ti_2Pn_2S behaves similarly. Ti_2Pn_2 is also capable of binding one, two, or three molecules of carbon monoxide. The bonding demands of a single CO molecule are incompatible with symmetric binding, and an asymmetric structure is found. The dicarbonyl adduct $Ti_2Pn_2(CO)_2$ has C_s symmetry with the Ti_2Pn_2 unit acting as two MCp_2 fragments. Synthetic studies showed that in the presence of excess CO the tricarbonyl complex $Ti_2Pn_2^{+2}(CO)_3$ is formed, which optimizes to an asymmetric structure with one semibridging and two terminal CO ligands. Low-temperature ^{13}C NMR spectroscopy revealed a rapid dynamic exchange between the two bound CO sites and free CO.



INTRODUCTION

Pentalene (Pn , C_8H_6) and its derivatives show a variety of coordination modes to transition metals.¹ When acting as a ligand, pentalene is formally classified as a dianion, $[C_8H_6]^{2-}$, or as an L_3X_2 ligand in the Covalent Bond Classification (CBC) method.^{2–4} To a certain extent, its coordination chemistry resembles that of cyclooctatetraene, which is also a member of the L_3X_2 class, but when coordinated to a single metal in an η^8 fashion it is nonplanar, folding around the two bridgehead carbons.^{5–7} Much progress has been made in synthesizing compounds so-called “double-sandwich” complexes, where two metals are sandwiched between two pentalene ligands. Early work by Katz employed unsubstituted pentalene forming M_2Pn_2 complexes with Co and Ni,^{8,9} but substituted pentalenes that offer solubility and steric protection have extended the number of these double sandwiches across the whole transition series.^{7,10–14} Computational studies using density functional theory (DFT) have established the metal–metal bond order in these bimetallic compounds.^{7,10–14} If the bridgehead carbons are treated as donating their two π electrons to both metals in a μ -L fashion, use of the 18 electron rule enables the metal–metal bond order to be predicted correctly¹⁵ (Figure 1) and

establishes that all except the Ti derivative are electronically saturated.

We have recently extended the series of known bis(pentalene) double-sandwich compounds to titanium using the silylated pentalene ligand $1,4\{-Si^iPr_3\}_2C_8H_4$ (Pn^+), and $Ti_2Pn_2^{+2}$ shows unique reactivity among pentalene double-

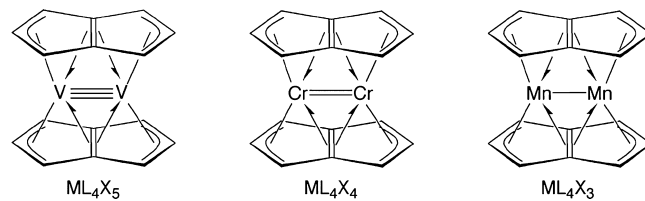


Figure 1. M–M bond orders predicted by assuming that the bridging pentalene is a five-electron L_2X donor to each metal (bottom); the allyl portion is an LX donor. The M–M bond orders predicted are in accord with theory. For clarity, pentalene substituents are not shown.

Received: April 29, 2015

Published: July 5, 2015

Table 1. Selected Calculated Structural Parameters (\AA , deg) for Optimized Structures^a

compound	Ti–Ti	Ti–Ct	Ct–Ti–Ct	Ti–C	Ti–O/S	C–O/S	O–Ti–O
Ti_2Pn_2 (1)	2.33, 2.34	2.01, 2.01	180, 180				
Ti_2Pn_2 (2)	2.37, 2.31	2.00, 2.03	153, 158				
Ti_2Pn_2^+ ($[\text{2}]^+$)	2.47, 2.43	2.03, 2.04	145, 147				
$\text{Ti}_2\text{Pn}_2\text{CO}_2$ (3)	2.41, 2.40	2.07, 2.10	141, 141	2.18, 2.14	2.27, 2.25	1.26, 1.29	
$\text{Ti}_2\text{Pn}_2\text{CS}_2$ (4)	2.43, 2.41	2.10, 2.11	138, 138	2.27, 2.24	2.54, 2.58	1.67, 1.72	
$\text{Ti}_2\text{Pn}_2\text{COS}$ (5)	2.41, 2.40	2.08, 2.09	140, 141	2.19, 2.17	2.19, 2.16	1.26, 1.29	
		2.09, 2.08	139, 140	2.25, 2.20	2.63, 2.69	1.68, 1.73	
$\text{Ti}_2\text{Pn}_2\text{CO}$ (6)	2.38, 2.36	2.06, 2.08	143, 143	2.04, 2.02	2.35, 2.26	1.21, 1.25	
$\text{Ti}_2\text{Pn}_2(\text{CO})_2$ (7)	2.42, 2.42	2.05, 2.05	144, 144	2.08, 2.08		1.17, 1.17	
			142, 144			1.17, 1.18	
$\text{Ti}_2\text{Pn}_2(\text{CO})_3$ (8)	2.63, 2.64	2.04, 2.07	143, 142	2.02, 1.99		1.17, 1.19	
		2.09, 2.11	137, 137	2.06, 2.05		1.17, 1.19	
				2.07, 2.03		1.16, 1.18	
$\text{Ti}_2\text{Pn}_2\text{O}$ (9)	2.38, 2.36	2.13, 2.14	139, 140		1.87, 1.85		79, 79
PnTiOTiPn ($S = 1$) (10)	3.40, 3.69	1.96, 1.99	57, 57		1.86, 1.85		133, 180
PnTiOTiPn ($S = 0$) (11)	2.88, 2.80	1.96, 1.99	57, 57		1.85, 1.83		103, 100
$\text{Ti}_2\text{Pn}_2\text{O}(\text{CO})$ (12)	2.46, 2.43	2.18, 2.17	135, 137	2.08, 2.07	1.76, 1.74	1.16, 1.17	
		2.11, 2.13	138, 138		2.10, 2.07		
$\text{Ti}_2\text{Pn}_2\text{S}$ (13)	2.44, 2.42	2.11, 2.12	137, 140		2.37, 2.39		62, 61
$\text{Ti}_2\text{Pn}_2\text{S}(\text{CO})$ (14)	2.48	2.12	135	2.08	2.30		61
		2.11	136		2.54		
$\text{PnTiO}_2\text{TiPn}$ (15)	2.74, 2.75	2.00, 2.02	56, 56		1.87, 1.85		95, 96

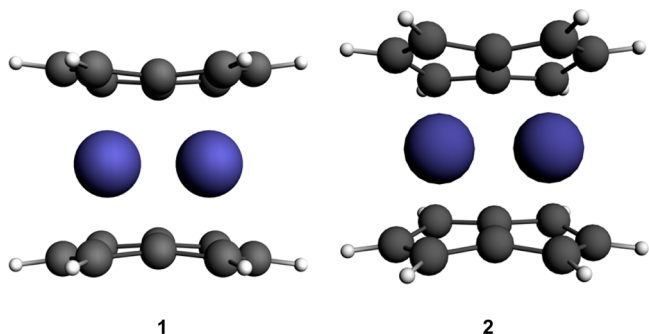
^aCt denotes the η^5 centroid of the Pn ring.

sandwich complexes, leading to a number of novel derivatives.^{16,17} The mechanism of the reaction of its CO_2 complex is described in the companion paper;¹⁷ here we examine the bonding in a range of derivatives in more detail.

RESULTS AND DISCUSSION

All of the calculations employed a model system with the pentalene substituents replaced by H atoms. Key structural parameters are given in Table 1. Optimized coordinates are given in the Supporting Information (SI). Numbers obtained by two different computational methods are given in normal text for ADF (BP/TZP) and in *italics* for Gaussian (B3LYP/SDD).

Ti₂(μ: η^5,η^5 -Pn)₂. Ti₂(μ: η^5,η^5 -Pn)⁺₂ has a bent structure.¹⁴ Optimizations of the structure of Ti₂(μ: η^5,η^5 -Pn)₂ (abbreviated Ti₂Pn₂) were carried out with D_{2h} symmetry (**1**) and no symmetry constraints (**2**).



Structure **1** had a low imaginary frequency (wavenumber/cm⁻¹ = -i80; -i69). Structure **2** had C_{2v} symmetry and was a local minimum; it had the same energy as structure **1** within computational error ([E(**2**) - E(**1**)]/kcal mol⁻¹ = -2;+1). The calculated Ti–Ti distances in **2** (2.37 Å, 2.31 Å) compare well with that found experimentally for Ti₂Pn₂⁺ (2.399(2) Å), as do

the calculated centroid–metal–centroid angles (153°, 158° calcd; 153.84(17)°, 156.6(2)° exptl) (Table 1). The short Ti–Ti distance indicates significant bonding between the Ti atoms.

The bonding in bis(pentalene)dimetal sandwiches has been discussed previously.^{7,10–14,18} The bent structure of Ti₂Pn₂ introduces a new motif and small modifications to the bonding.¹⁴ Figure 2 shows isosurfaces for the metal-based frontier molecular orbitals (MOs) for both **1** and **2**. Four electrons occupy these frontier orbitals, resulting in a double bond between the Ti atoms. Upon lowering of the symmetry from D_{2h} to C_{2v}, the highest occupied MO (HOMO) and the HOMO-1 become the same symmetry and mix, with the consequence that the orbitals appear as two bent bonds, equivalent to a σ bond and a π bond. The lowest-occupied MO (LUMO), which is doubly occupied in the vanadium analogue,¹² is only weakly metal–metal bonding because of small overlap. The three a₁ metal-based orbitals form the principal frontier orbitals of Ti₂Pn₂. In addition, the higher-lying unoccupied orbitals of b symmetry are metal–metal antibonding and provide additional flexibility for bonding of additional ligands.

The three frontier orbitals with a₁ symmetry may also be formed by in-phase combinations of the well-known frontier orbitals of two bent metallocenes (Figure 3).^{19–24}

The closeness in energy of the two structures demonstrates that there is no strong driving force toward the bent structure. Indeed, most of the orbitals rise marginally in energy in going from **1** to **2**. The one orbital that shows a significant lowering in energy is a member of the metal–ligand bonding set, shown in Figure 4. The orbitals derived from the upper occupied orbitals of the pentalene dianion, π4 and π5, are the principal orbitals used in metal–ligand bonding. In D_{2h} symmetry, two linear combinations, 4a_u and 8b_{1u}, mix well with the metal d orbitals. The other two linear combinations, Sb_{1g} and 9a_g, have poor overlap with the metal set. Bending the molecule and lowering the symmetry improve the overlap for the Sb_{1g} orbital, which

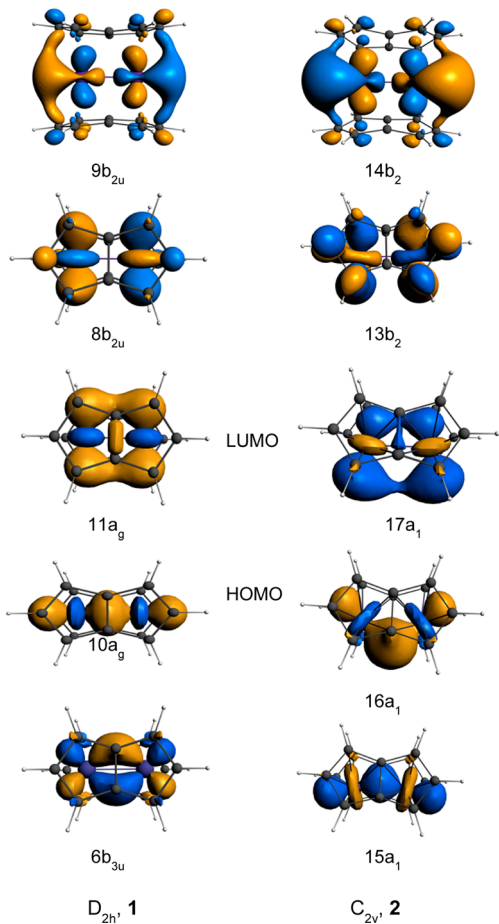


Figure 2. Frontier MOs of Ti_2Pn_2 with D_{2h} symmetry (**1**) and C_{2v} symmetry (**2**).

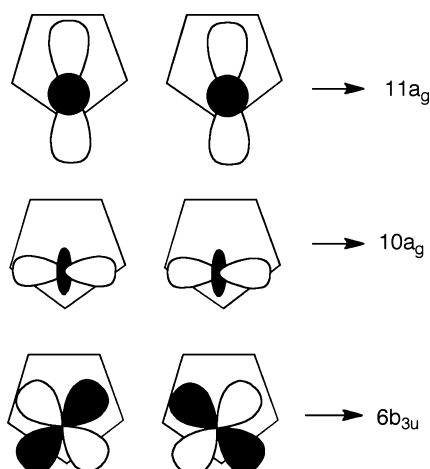


Figure 3. Derivation of the frontier orbitals of Ti_2Pn_2 from those of two metallocenes.

becomes the $12b_2$ orbital in C_{2v} symmetry, and its energy decreases. This situation is reminiscent of the effect of bending in parallel metallocenes.²⁵

Electrochemical Studies. Cyclic voltammetry (CV) of $\text{Ti}_2\text{Pn}^{\dagger}_2$ was carried out to assess the stability of the mixed-valence form of the bimetallic complex and to choose an appropriate chemical redox agent for its preparation on a synthetic scale.

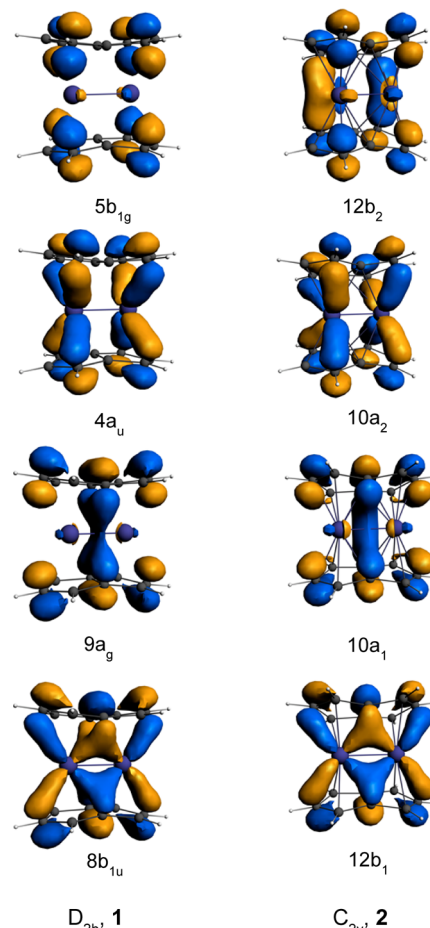


Figure 4. MOs of **1** and **2** derived from π_5 and π_4 of pentalene.

CV of $\text{Ti}_2\text{Pn}^{\dagger}_2$ in THF/0.1 M [$^{t}\text{Bu}_4\text{N}][\text{PF}_6]$] revealed two major redox processes within the electrochemical window, as shown in Figure 5; the data are summarized in Table 2. Process I, centered at $E_{1/2} = -2.48$ V vs $\text{FeCp}_2^{+/-}$, is assigned to a reduction to the monoanion $[\text{Ti}_2\text{Pn}^{\dagger}_2]^-$. Repetitive potential

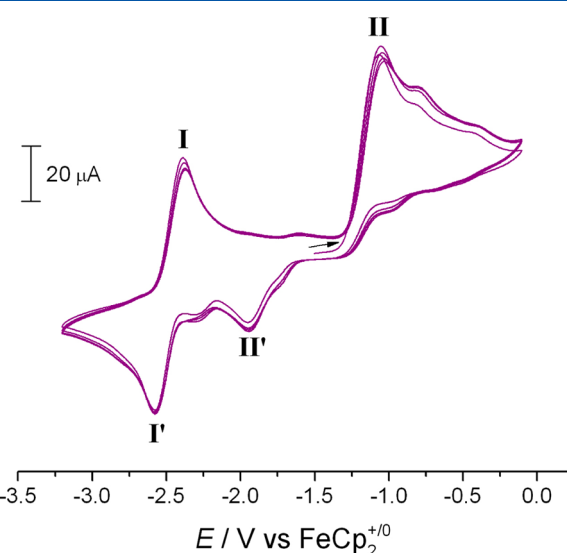


Figure 5. Overlaid CV scans (three cycles) for $\text{Ti}_2\text{Pn}^{\dagger}_2$ in THF/0.1 M [$^{t}\text{Bu}_4\text{N}][\text{PF}_6]$ at a scan rate of 100 mV s^{-1} .

Table 2. Peak Potentials (E_p) and Limiting Currents (i_p) for the CV of $Ti_2Pn_2^+$ in THF/0.1 M $[^nBu_4N][PF_6]$ at a Scan Rate of 100 mV s⁻¹

	process I	process II
E_{pa}/V vs $FeCp_2^{+/-}$	-2.38	-1.06
E_{pc}/V vs $FeCp_2^{+/-}$	-2.58	-1.95
$E_{1/2}/V$ vs $FeCp_2^{+/-}$	-2.48	n/a
$\Delta E_{pp}/mV$	201	893
i_{pa}/i_{pc}	1.0	3.0

cycling over process I in isolation using variable scan rates from 100 to 1000 mV s⁻¹ (see the SI), showed electrochemical behavior best described as quasi-reversible.²⁶ The peak-to-peak separation (ΔE_{pp}) is similar to that for ferrocene under the same conditions (ca. 200 mV), suggesting the transfer of one electron. For comparison, the permethylpentalecene double-sandwich complexes $M_2Pn_2^*$ ($M = V, Cr, Mn, Co, Ni; Pn^* = C_8Me_6$) studied by O'Hare and co-workers show a single-electron reduction process with electrode potentials ranging from -2.75 to -1.85 V vs $FeCp_2^{+/-}$.¹² Process II is assigned to a one-electron oxidation with a peak potential (E_{pa}) of -1.06 V vs $FeCp_2^{+/-}$ in the forward scan, and an associated cathodic wave was observed at $E_{pc} = -1.95$ V vs $FeCp_2^{+/-}$ in the reverse scan. Irreversible behavior suggests that the product of this oxidation, $[Ti_2Pn_2^+]^+$, is not stable under the conditions and time scale of the CV experiment. The mononuclear bis(cyclopentadienyl)titanium sandwich complexes studied by Chirik and co-workers also showed irreversible voltammetric responses in THF/ $[^nBu_4N][PF_6]$.²⁷ The oxidation of the double-sandwich complex $Ti_2Pn_2^+$ occurs at a relatively cathodic potential (-1.06 V vs $FeCp_2^{+/-}$), consistent with an electron-rich complex that can act as a reducing agent for substrates such as CO₂.

Employing $[^nBu_4N][B(C_6F_5)_4]$ as the supporting electrolyte resulted in better-resolution CV data for $Ti_2Pn_2^+$ in oxidative scans compared with $[^nBu_4N][PF_6]$ (see Figure S3 in the SI), and a further quasi-reversible oxidation, process III, was observed at $E_{1/2} = -0.54$ V vs $FeCp_2^{+/-}$. The $[B(C_6F_5)_4]^-$ anion is well-known for its lower ion-pairing capability (spherical diameters: $[B(C_6F_5)_4]^- = 10$ Å; $[PF_6]^- = 3.3$ Å),²⁸ which is beneficial for the study of multielectron processes with positively charged analytes,²⁹ and it was therefore chosen for the large-scale synthesis of the cationic species.

[$Ti_2(\mu\eta^5,\eta^5-Pn^*)_2[B(C_6F_5)_4]$. Reaction of $Ti_2Pn_2^+$ with the mild oxidizing agent $[FeCp_2^*][B(C_6F_5)_4]$ at -35 °C resulted in a brown suspension. Following evaporation of the solvent and removal of $FeCp_2^*$, the residues were recrystallized from a concentrated Et₂O/hexane solution at -35 °C to obtain $[Ti_2(\mu:\eta^5,\eta^5-Pn^*)_2][B(C_6F_5)_4]$ in 55% yield, which was fully characterized by spectroscopic and analytical methods. The cation $[Ti_2Pn_2^+]^+$ is, to the best of our knowledge, the first example of a formally a Ti(II)-Ti(III) mixed-valence species. The molecular structure (Figure 6) reveals a “naked” double-sandwich cation with no close contacts between the anion and the metal–metal bonded core.

The most noteworthy structural feature is the longer Ti–Ti bond distance in $[Ti_2Pn_2^+][B(C_6F_5)_4]$ (2.5091(9) Å) compared with $Ti_2Pn_2^+$ (2.399(2) Å). This elongation is consistent with the removal of an electron from the M–M bonding HOMO (16a₁) in the molecular orbital scheme for Ti_2Pn_2 (Figure 2). There is no significant difference in the Ti–C and pentalecene C–C bond lengths in $Ti_2Pn_2^+$ relative to $[Ti_2Pn_2^+]^+$, but the

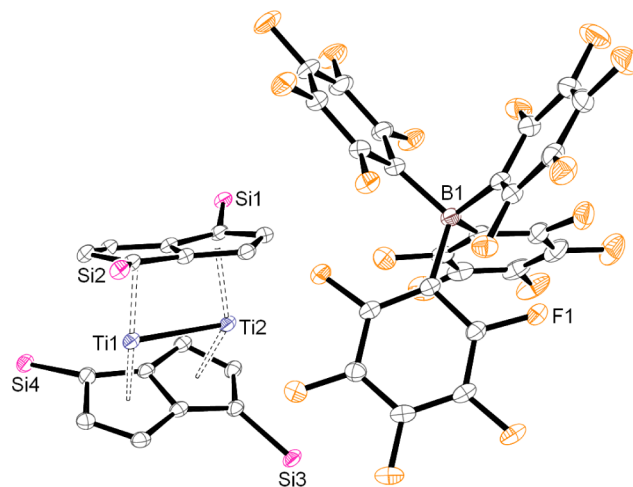


Figure 6. Displacement ellipsoid plot (30% probability) of $[Ti_2Pn_2^+][B(C_6F_5)_4]$. H atoms and ¹Pr groups have been omitted for clarity. Selected structural parameters (Å, deg): Ti1–Ti2 = 2.5091(9), Ti–C_{ring}^a = 2.0233(14), Ti–C_{ring}^a = 2.384(3), C–C_{ring}^a = 1.437(4), Ti1–B1 = 7.134(4), Ct–Ti–Ct^a = 142.38(6), ring slippage^a = 0.105(3), twist angle = 14.44(9), hinge angle = 5.5(3), fold angle = 8.38(13). Ct denotes the η^5 centroid of the Pn ring. ^aAverage value.

pentalene ligands bend around the Ti₂ core to a greater extent in the cationic complex; the centroid–metal–centroid angles around Ti1 and Ti2 are 142.28(6)° and 142.48(6)°, respectively, compared with the respective angles of 153.84(17)° and 156.6(2)° in the neutral complex. The decamethyltitanocene cation in $[Cp^*_2Ti][BPh_4]$ ³⁰ also adopts a more bent structure than the neutral titanocenes.^{31,32}

As expected, $[Ti_2Pn_2^+][B(C_6F_5)_4]$ is paramagnetic; the ¹H, ¹³C, and ²⁹Si NMR spectra in THF-*d*₈ were broad and uninformative, but the ¹⁹F and ¹¹B{¹H} NMR spectra showed well-resolved signals at δ_F -132.7, -165.2, and -168.7 and δ_B -14.75, respectively, attributable to the outer-sphere tetrakis-(perfluorophenyl)borate anion. The solution-phase magnetic moment of $[Ti_2Pn_2^+][B(C_6F_5)_4]$ determined by the Evans method was 1.96 μ_B per dimer,^{33,34} which is slightly greater than the spin-only moment for one unpaired electron (1.73 μ_B). Comparable data were observed in the solid state by SQUID magnetometry ($\mu_{eff}(260\text{ K}) = 1.92\mu_B$ per dimer; see Figure S4 in the SI).

The electron paramagnetic resonance (EPR) spectra of $[Ti_2Pn_2^+][B(C_6F_5)_4]$ were consistent with an $S = 1/2$ ground-state electronic configuration. The X-band spectrum of a polycrystalline sample at room temperature (Figure 7) showed an axial signal with two principal *g* values simulated ($g_{\perp} = 2.003$ and $g_{\parallel} = 1.944$), giving an average *g* value of 1.964. The large line widths ($\Delta B_{\perp} = 24.5$ G and $\Delta B_{\parallel} = 23$ G) meant that any hyperfine structure and further *g* anisotropy were not resolved.

[$Ti_2Pn_2^+$]. Calculations on the cation $[Ti_2Pn_2^+]([2]^+)$ show a lengthening of the Ti–Ti distance by ca. 0.1 Å and an increase in the bending of the pentalecene ligands around the Ti₂ core (Table 1), as found experimentally for the silylated analogues. The orbital manifold shows the expected hole in the 16a₁ orbital (Figure 2), which is delocalized over the Ti atoms. The principal *g* values calculated for $[2]^+$ are $g_x = 1.956$, $g_y = 2.000$, $g_z = 2.008$. Their relative magnitude and ordering ($g_x < g_y \approx g_z$) explain the apparent axial symmetry of the experimental EPR spectrum, with the *C*₂ axis perpendicular to the *x* axis (in a coordinate system with the *x* axis passing through the pentalene

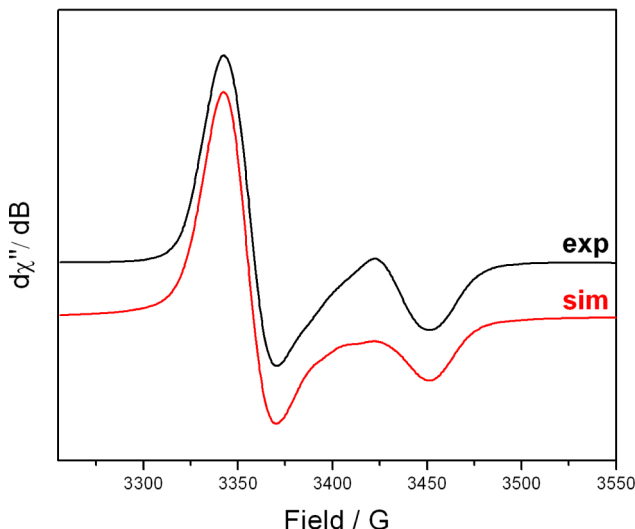
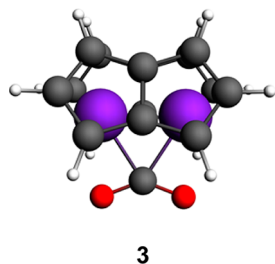


Figure 7. X-band EPR spectrum of polycrystalline $[\text{Ti}_2\text{Pn}^\dagger_2]^2[\text{B}(\text{C}_6\text{F}_5)_4]$ at room temperature (black line) and corresponding simulation (red line).

bridgehead C–C bonds), and are consistent with a singly occupied MO (SOMO) $16a_1$ (Figure 2).

Ti₂(μ : η^5,η^5 -Pn)₂CO₂. The CO₂ adduct Ti₂(μ : η^5,η^5 -Pn)₂CO₂ has been spectroscopically characterized in solution at low temperature but is too unstable to be isolated.¹⁷ Optimizing the geometry of Ti₂Pn₂CO₂ from various starting geometries led to a minimum-energy structure with C_{2v} symmetry (3). Selected geometric parameters are given in Table 1.



The Ti–Ti distance is short (2.41 Å), indicating strong bonding between the Ti atoms. The pentalene rings are bent back slightly more than in Ti₂Pn₂. Examination of the MOs of 3 (Figure 8) shows that the key bonding interaction is between the LUMO of bent CO₂ and primarily the HOMO of 2 ($16a_1$) to form a stabilized orbital, $18a_1$, that is 2.4 eV more stable than the Ti–Ti bonding orbital. In localized bonding terms, the two M–M bonds are replaced by one M–M bond and a three-center, two-electron (3c-2e) bond linking the C of the CO₂ to the M atoms. The two O atoms have a favorable but weak interaction with the Ti atoms, accounting for the relatively long Ti–O distance (2.27 Å).

Further insight into the binding of CO₂ is given by a fragment analysis. Upon bending of CO₂, the LUMO is of a_1 symmetry and acts as an acceptor orbital. The CO₂ HOMO and HOMO–1, located on the O atoms, are of a_2 and b_2 symmetry. Thus, donation from these into the LUMO of Ti₂Pn₂, which is of a_1 symmetry, is forbidden. Fragment analysis enables the energies of the bonding interactions of the Ti₂Pn₂ fragment with the CO₂ fragment to be separated according to symmetry. The energies attributable to the various interactions are given in Table 3. The energy values confirm that donation

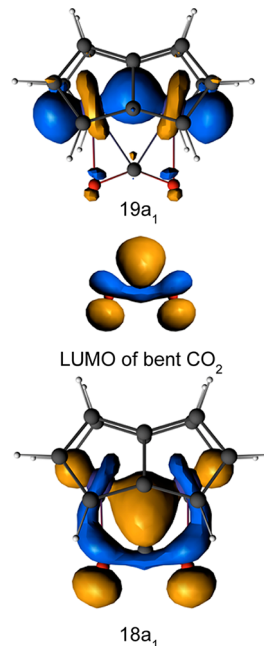


Figure 8. Ti–Ti bonding orbital of Ti₂Pn₂CO₂ ($19a_1$), the LUMO of bent CO₂, and the bonding orbital ($18a_1$) resulting from nucleophilic attack of Ti₂Pn₂ on CO₂.

Table 3. Energies (in eV) of Orbital Interactions Divided According to Their Symmetries; The Various Molecules with C_{2v} Symmetry Are Divided into Ti₂Pn₂ and Ligand Fragments

	3	4	7	9	13
A ₁	−116	−192	−81	−186	−80
A ₂	−2	−4	−15	0	−1
B ₁	−7	−8	−8	−136	−100
B ₂	−15	−21	−24	−165	−125

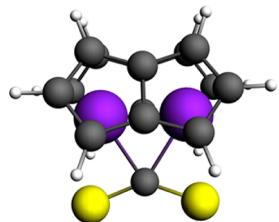
from the HOMO of Ti₂Pn₂ is the predominant bonding interaction. The occupancies of the LUMO, HOMO, and HOMO–1 of the Ti₂Pn₂ fragment in 3 are given in Table 4.

Table 4. Occupancies of the Fragment Orbitals of Ti₂Pn₂ in the Molecular Calculations for 2, 3, 4, 5, 6, 7, 8, 9, and 13

	14b ₂	13b ₂	17a ₁	16a ₁	15a ₁
2	0	0	0	2.00	2.00
3	0.07	0.09	0.18	0.98	1.99
4	0.22	0.14	0.29	0.77	1.97
5	0.13	0.12	0.23	0.89	1.98
6	0.02	0.07	0.57	1.02	2.00
7	0	0	0.39	1.31	1.97
8	0.33	0.83	0.56	0.70	1.43
9	0.03	0.10	0.12	0.42	1.46
13	0.11	0.25	0.06	0.67	1.97

Some remixing between the HOMO and LUMO does occur, but on the whole the HOMO–1 of Ti₂Pn₂ retains its integrity to form the HOMO of the CO₂ derivative, $19a_1$ (Figure 8). Thus, CO₂ may be regarded as acting as a μ -Z ligand.

Ti₂(μ : η^5,η^5 -Pn)₂CS₂. The adduct of CO₂ to Ti₂Pn₂⁺ has not been structurally characterized, but the product of CS₂ addition has.¹⁷ Geometry optimization of Ti₂Pn₂CS₂ led to structure 4, analogous to 3. Key structural parameters are given in Table 1,



4

and selected MOs are shown in Figure 9. The Ti–Ti distance is again consistent with significant Ti–Ti bonding. The Ti–C

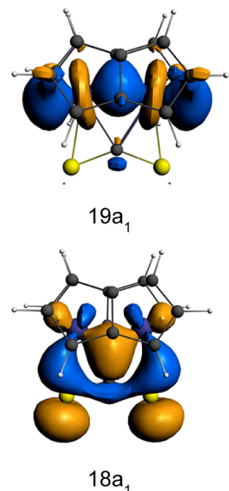
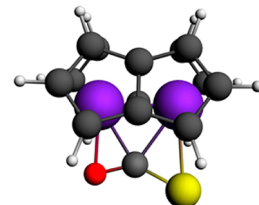


Figure 9. Ti–Ti bonding orbital ($19a_1$) and Ti_2 – CS_2 bonding orbital ($18a_1$) of $Ti_2Pn_2CS_2$ (**4**).

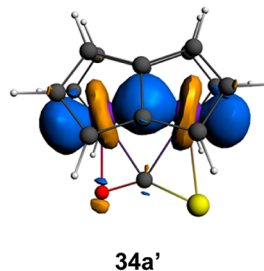
distance is 0.09 Å longer than in the CO_2 analogue. The Ti–S distance is 0.27 Å longer than the Ti–O distance, whereas the covalent radii differ by 0.39 Å,³⁵ indicating a more significant interaction with Ti for S than for O. The angles at C are very similar (137° in **3**, 138° in **4**).

Upon coordination of CS_2 , one Ti–Ti bonding orbital, $19a_1$, remains intact, as is the case for the CO_2 complex. The orbital $18a_1$ that is responsible for CS_2 binding is more delocalized and multicentered than the analogue in **3**, consistent with the differences in distance discussed above. Sulfur, with its higher-energy orbitals, has a stronger interaction with the Ti atoms. The fragment analysis reinforces this view. Not only is the a_1 interaction energy greater than for **3** (Table 3), but there is also greater Ti_2Pn_2 HOMO–LUMO mixing, indicating both donor and acceptor quality in the bonding interaction (Table 4). The higher-lying orbitals of b_2 symmetry have greater fragment occupancy in **4** than in **3** (Table 4), denoting donation from the b_2 HOMO of bent CS_2 . Examination of the overlap population matrices for the two molecules gives a value of 0.19 for **4**, which is significantly greater than the value of 0.05 for **3**. Comparison of the calculated charges on O and S in the two molecules also reinforces the view that S is a better donor having a less negative charge (O –0.60, S –0.09 Mulliken; O –0.21, S –0.05 Hirshfeld; O –0.20, S –0.08 Voronoi).

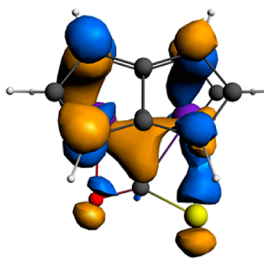
Ti₂Pn₂COS. The COS adduct, **5**, has been identified in solution but not isolated, as it undergoes rapid decomposition below room temperature.¹⁷ The HOMO, $34a'$, is yet again a Ti–Ti bonding orbital that is relatively unperturbed upon binding of COS (Figure 10). The closeness in energy of the



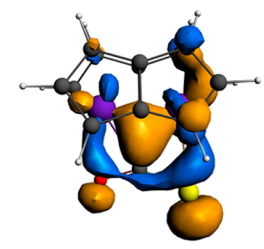
5



34a'



33a'



32a'

Figure 10. Top three occupied orbitals of Ti_2Pn_2COS (**5**).

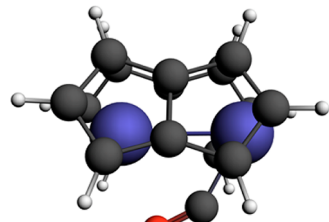
Ti_2COS bonding orbital to the $12b_1$ orbital of the Ti_2Pn_2 pentalene unit leads to mixing of these two orbitals to form the $33a'$ and $32a'$ MOs (Figure 10); the lower symmetry caused by COS enables this mixing to take place. The fragment calculation (Table 4) reveals a situation for **5** intermediate between **3** and **4**. The binding energies of the triatomic ligands to Ti_2Pn_2 decrease in the order $CS_2 > COS > CO_2$ (Table 5).

Ti₂Pn₂CO. On the basis of the nature of CO as a π -acceptor ligand, symmetric bridging of the two Ti centers by CO is not favored because the high-lying occupied frontier orbitals of Ti_2Pn_2 are of the wrong symmetry. The structure of Ti_2Pn_2CO (**6**) has C_s symmetry with the CO bound sideways-on to the Ti_2 core, in agreement with the experimentally determined structure of the monocarbonyl complex $Ti_2(\mu:\eta^5,\eta^5-Pn^\dagger)_2CO$.¹⁷

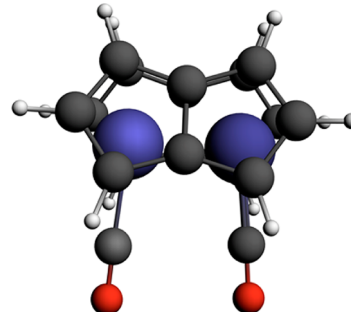
Inspection of the orbitals of **6** (Figure 11) indicates that the positioning of CO is steered by back-donation from the HOMO of the Ti_2Pn_2 fragment. Once again a Ti–Ti bond is retained, forming the HOMO of **6**, $55a$. The composition of

Table 5. Calculated SCF Energies (ΔE) and Standard Free Energies (ΔG°) (in kcal mol⁻¹) for Binding of Ligands to the Ti_2Pn_2 Unit

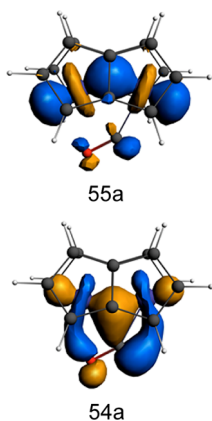
compound	ligand(s)	ΔE	ΔG°
3	CO_2	-53	-37
4	CS_2	-70	-52
5	COS	-61	-44
6	CO	-48	-31
7	$(CO)_2$	-74	-43
8	$(CO)_3$	-94	-50
12	CO	-19	-5
14	CO	-25	-3



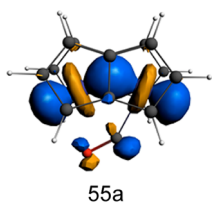
6



7



54a



55a

Figure 11. HOMO and HOMO-1 of Ti_2Pn_2CO (6).

the top two occupied orbitals in terms of their fragment orbitals is given in Table 4. The HOMO-1, 54a, is composed of one of the 5π orbitals of CO and orbital 16a₁ of 2. The calculated wavenumber for the CO stretch is rather lower than the range for symmetric bridging carbonyls but in good agreement with the experimental value (Table 6).

$Ti_2Pn_2(CO)_2$. Geometry optimization of the dicarbonyl adduct $Ti_2Pn_2(CO)_2$ by both computational methods gave a structure of C_s symmetry only slightly displaced from C_{2v} symmetry, 7. The ADF-calculated structure had an imaginary frequency of a' symmetry with a wavenumber of $-i15\text{ cm}^{-1}$. The calculated geometry agrees well with that found experimentally.¹⁶

The Ti–Ti bonding orbital, 36a (Figure 12) remains intact, consistent with the short Ti–Ti distance of 2.42 Å, but it is straighter than those found for the other derivatives. Back-bonding to both CO groups occurs in orbital 35a, which has clear origins in the 6b_{3u} orbital of 1.

The agreement between the experimental and calculated stretching wavenumbers (Table 6) follows the same pattern as for the monocarbonyl, 6. Although binding of CO to 6 is energetically favorable, the ligand redistribution of 6 to afford 7 and 2 in the absence of CO is not predicted to be spontaneous (Table 5).

$Ti_2Pn_2^{\dagger}(CO)_3$. It was previously observed that reaction of $Ti_2Pn_2^{\dagger}$ with excess CO at $-78\text{ }^\circ\text{C}$ produced an orange-brown solution, which following removal of the reaction headspace in vacuo and warming to room temperature resulted in a color

Table 6. Experimental and Calculated (ADF and Gaussian) Wavenumbers (cm⁻¹) for Selected Stretching Vibrations

compound	mode	experimental	calculated
$Ti_2Pn_2CO_2$ (3)	$\nu(CO)$	solution: 1678, 1236	1669 (w), 1214 (w) 1601 (w), 1193 (w)
Ti_2Pn_2CO (6)	$\nu(CO)$	solid: 1655 solution: not observed	1644 (w) 1532 (w)
$Ti_2Pn_2(CO)_2$ (7)	$\nu(CO)$	solid: 1987 (s), 1910 (m) solution: 1991 (s), 1910 (w)	1947 (s), 1878 (m) 1899 (s), 1810 (m)
$Ti_2Pn_2(CO)_3$ (8)	$\nu(CO)$	solution: 1991 (w), 1910 (s)	1941 (s), 1894 (s), 1873 (w) 1918 (s), 1868 (s), 1835 (w)
$Ti_2Pn_2O(CO)$ (9)	$\nu(CO)$	not observed	1954 (s) 1942 (s)
$Ti_2Pn_2CS_2$ (4)	$\nu(CS)$	solid: 1101 solution 1104	1079 (w)
Ti_2Pn_2COS (5)	$\nu(CO)$	solution: 1498	1487 (w) 1428 (w)
$Ti_2Pn_2S(CO)$ (14)	$\nu(CO)$	solution: 2011	1937 (m) 1924 (m)

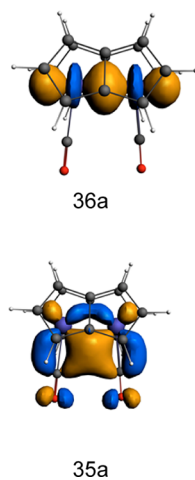


Figure 12. HOMO and HOMO-1 of $\text{Ti}_2\text{Pn}_2(\text{CO})_2$ (7).

change to green-brown, characteristic of the dicarbonyl complex $\text{Ti}_2\text{Pn}_2^{\dagger}(\text{CO})_2$.¹⁶ These observations hinted that an additional product is formed in the presence of excess CO at low temperatures, which was investigated by variable-temperature (VT) NMR spectroscopy. A solution of $\text{Ti}_2\text{Pn}_2^{\dagger}(\text{CO})_2$ in methylcyclohexane- d_{14} was sealed under ^{13}CO , and the $^{13}\text{C}\{^1\text{H}\}$ NMR spectrum at 30 °C (Figure 13) showed a very

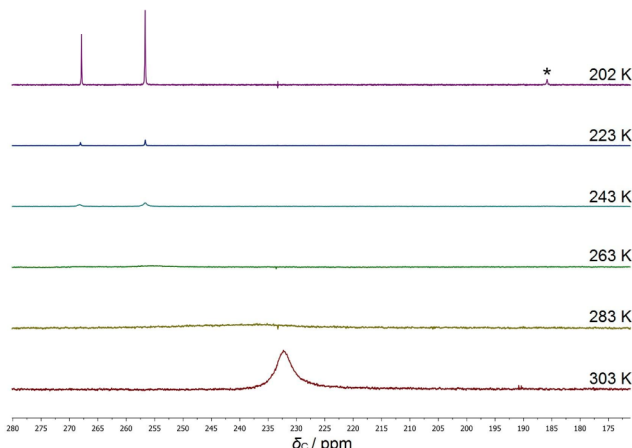
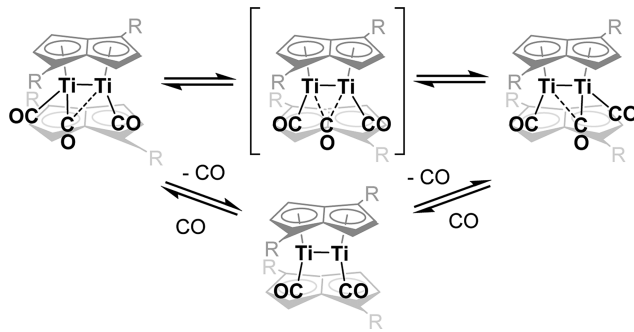


Figure 13. Selected VT $^{13}\text{C}\{^1\text{H}\}$ NMR spectra of $\text{Ti}_2\text{Pn}_2^{\dagger}(\text{CO})_3$ in $\text{MeCy}-d_{14}$ solution (the temperature increases down the page in 20 K increments). The asterisk indicates free ^{13}CO .

broad resonance centered at 232 ppm ($\Delta\nu_{1/2} = 190$ Hz). The spectrum was resolved by cooling to −70 °C (Figure 13), with two peaks in a ca. 2:1 ratio at 268 and 257 ppm, assigned to two chemically inequivalent carbonyl environments in $\text{Ti}_2\text{Pn}_2^{\dagger}(\text{CO})_3$, and a peak at 186 ppm, corresponding to free ^{13}CO in solution. These three ^{13}C peaks broaden upon warming and coalesce at 0 °C (Figure 13), consistent with a dynamic intermolecular exchange process with free ^{13}CO . A ^{13}C – ^{13}C EXSY experiment at −40 °C (mixing time = 500 ms) showed cross-peaks between the bridging and terminal carbonyl signals, which implies that an exchange process between these CO sites also occurs in $\text{Ti}_2\text{Pn}_2^{\dagger}(\text{CO})_3$ (Scheme 1).

The carbonylation of $\text{Ti}_2\text{Pn}_2^{\dagger}$ in methylcyclohexane solution at −55 °C was studied by in situ IR spectroscopy, which showed initial growth of an IR band at 1992 cm^{−1} that then

Scheme 1. Reactivity of $\text{Ti}_2\text{Pn}_2^{\dagger}(\text{CO})_2$ with CO (R = Si*i*Pr₃)



decreased in intensity and leveled off as a $\nu(\text{CO})$ stretch at 1910 cm^{−1} grew in (Figure 14). This lower-energy $\nu(\text{CO})$

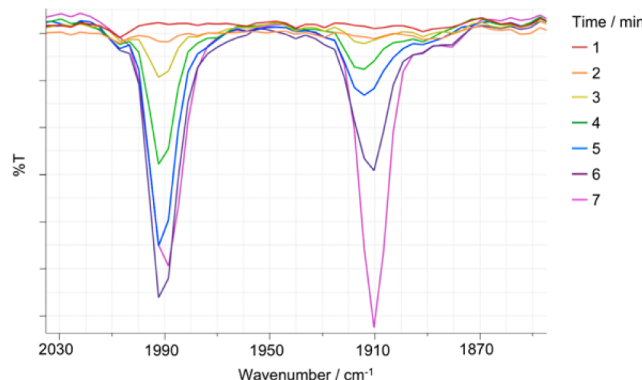


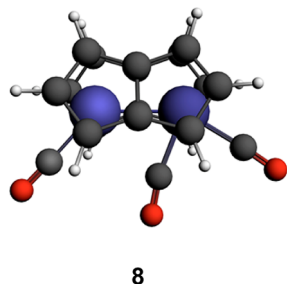
Figure 14. $\nu(\text{CO})$ region of the ReactIR spectrum of $\text{Ti}_2\text{Pn}_2^{\dagger}$ with CO at −55 °C.

stretch became the major IR band at −55 °C once gas addition was complete. At 26 °C under CO, the intensities of the two bands reversed, with 1992 cm^{−1} as the major $\nu(\text{CO})$ stretching band. Removal of the CO headspace in vacuo led to near complete removal in the lower-energy $\nu(\text{CO})$ stretch at 1910 cm^{−1} (see Figure S9 in the SI). These results suggest that the band centered at 1992 cm^{−1} is due to $\text{Ti}_2\text{Pn}_2^{\dagger}(\text{CO})_2$, which is the major product in the initial stages of reaction and upon warming to 26 °C when CO becomes less soluble. The IR band at 1910 cm^{−1} is assigned to the terminal $\nu(\text{CO})$ stretch in $\text{Ti}_2\text{Pn}_2^{\dagger}(\text{CO})_3$, which is the major product in solution under excess CO at −55 °C but diminishes upon exposure to vacuum and warming to room temperature. An analogous experiment performed using ^{13}CO gave similar qualitative results, with IR bands at 1948 and 1867 cm^{−1} assigned to the terminal $\nu(\text{CO})$ in $\text{Ti}_2\text{Pn}_2^{\dagger}(\text{CO})_2$ and $\text{Ti}_2\text{Pn}_2^{\dagger}(\text{CO})_3$, respectively. IR bands for the bridging CO ligands, expected in the region 1850–1600 cm^{−1},³⁶ were not observed in the solution spectra for $\text{Ti}_2\text{Pn}_2^{\dagger}(\text{CO})$ and $\text{Ti}_2\text{Pn}_2^{\dagger}(\text{CO})_3$, possibly because of extensive broadening.

Orange crystals of $\text{Ti}_2\text{Pn}_2^{\dagger}(\text{CO})_3$ were grown under an atmosphere of CO from a saturated toluene solution stored at −80 °C. Unfortunately, analysis by single-crystal X-ray diffraction was hampered by their deterioration when placed in oil for mounting, with effervescence of gas accompanying decomposition of the crystals. However, elemental analysis of the orange crystals was consistent with the proposed formulation of $\text{Ti}_2\text{Pn}_2^{\dagger}(\text{CO})_3$.

Ti₂Pn₂(CO)₃. Experimental evidence for a tricarbonyl species prompted the search for a computational analogue,

$\text{Ti}_2\text{Pn}_2(\text{CO})_3$, which optimized to structure 8. The Ti–Ti distance in 8 is significantly longer than those found in



structures 1–7. The structure is asymmetric with one semibridging and two terminal carbonyls. The two highest occupied orbitals, 65a and 64a (Figure 15) are principally

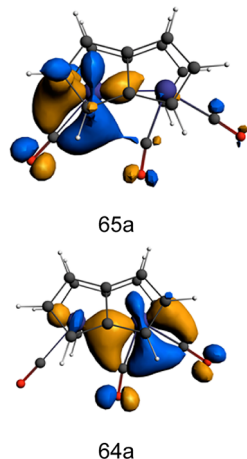


Figure 15. Ti–CO backbonding orbitals of $\text{Ti}_2\text{Pn}_2(\text{CO})_3$ (8).

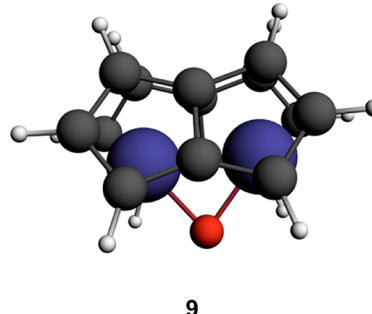
involved in back-donation to the CO ligands. The HOMO, 65a, is focused on the Ti, with just one bound CO contributing a π^* orbital. MO 64a binds the other two CO ligands but retains a small amount of Ti–Ti bonding character.

The Ti_2Pn_2 fragment occupations are in accord with the reduction in metal–metal bonding (Table 4). The occupancy of the 15a_1 Ti–Ti bonding orbital is reduced compared with the examples above, showing that in the case of 8 both Ti–Ti bonding orbitals of Ti_2Pn_2 are involved in back-donation. In addition, the occupancies of the LUMO+1 and LUMO+2 (13b_2 and 14b_2) are significant, and these have Ti–Ti antibonding character. The calculated CO stretching wave-numbers (Table 6) suggest that one of the three expected vibrations is coincident with the higher stretching frequency of the dicarbonyl. The second one, of lower energy, is stronger than the lower stretch of the dicarbonyl, and the third is too weak to be observed. These predictions fit well with the dynamic behavior of $\text{Ti}_2\text{Pn}_2^\dagger(\text{CO})_3$ in the spectroscopic studies described above.

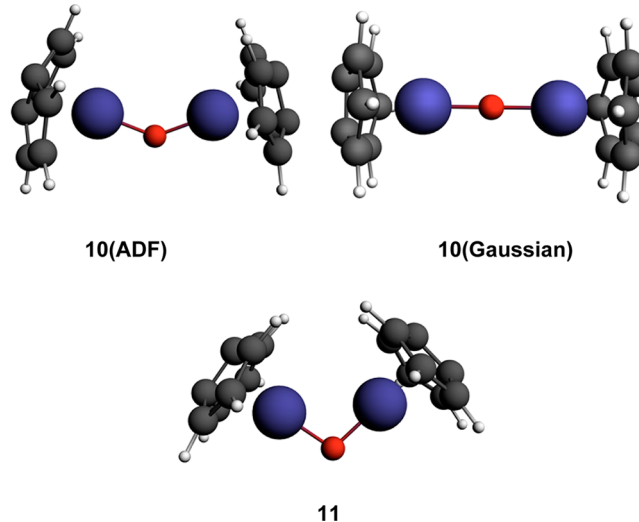
If $\text{Ti}_2\text{Pn}_2^\dagger(\text{CO})_3$ also has three inequivalent carbonyls, as suggested by the computed structure 8, three ^{13}CO signals are expected in the low-temperature NMR spectrum. As reported above, at $-70\text{ }^\circ\text{C}$ only two are observed (Figure 13). The obvious inference is that the two outer CO groups are rendered chemically equivalent on the NMR time scale by means of oscillation of the inner CO between them in what might be described as a “ping-pong” mechanism (see Scheme 1). It is

proposed that the exchange between bridging and terminal CO sites occurs indirectly via an intermolecular process.

Ti₂Pn₂O. Decomposition of $\text{Ti}_2\text{Pn}_2^\dagger\text{CO}_2$ proceeds via a mono(oxo) product, which can be synthesized independently by action of N_2O on $\text{Ti}_2\text{Pn}_2^\dagger$.¹⁷ Maintenance of the sandwich structure of the Ti_2Pn_2 fragment leads to a local minimum with C_{2v} symmetry, structure 9. With η^8 coordination of Pn to Ti, two other structures were found, one with a triplet state (10) and the other with a singlet state (11).



The structures found for the triplet state by the two methods differed in the Ti–O–Ti angle. ADF calculations optimized to a bent Ti–O–Ti unit, while the Gaussian calculations gave a linear Ti–O–Ti unit. Similar structures were found for the singlet state with η^8 coordination by the two computational methods (Table 1).



The energies of the three structures are close, and which one is the most stable is method- and temperature-dependent (Table 7). ADF (BP/TZP) shows the sandwich structure to be the most stable. Gaussian (B3LYP/SDD) estimates the SCF energy of the sandwich structure to be the lowest, but the free energy at 298 K shows the triplet η^8 -coordinated structure to be the most stable. This is in agreement with experiment, as the

Table 7. Relative Energies (kcal mol⁻¹) of Structures Found for $\text{Ti}_2\text{Pn}_2\text{O}$

compound	$\Delta E(\text{SCF})$	ΔH_{298}°	ΔG_{298}°
10	0, 0	0, 0	0, 2
11	12, 4	13, 3	8, 0
12	12, 19	13, 21	10, 20

sandwich structure is known to convert to the triplet state at room temperature.¹⁷

Structure **9** has a Ti–Ti bonding orbital, $17a_1$ (Figure 16). The high symmetry of the molecule facilitates identification of

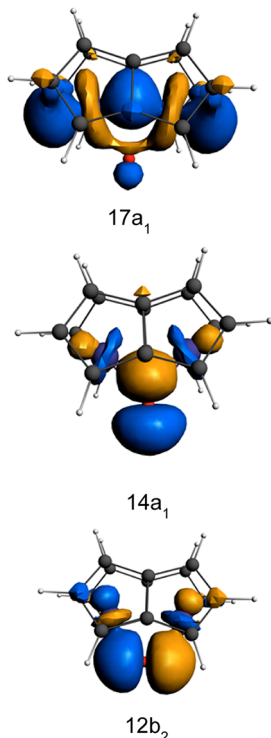


Figure 16. Ti–Ti and Ti–O bonding orbitals of $\text{Ti}_2\text{Pn}_2\text{O}$ (**9**).

orbitals associated with Ti–O bonding, $14a_1$ and $12b_2$. All three 2p orbitals of O contribute to its bonding, as illustrated by the binding energies decomposed by the symmetry of the orbitals involved (Table 3). The O atom competes effectively with the pentalene ligands for the Ti 3d orbitals, as evidenced by the increased Ti ring centroid distances (Table 1).

Orbitals containing the metal-based electrons of **10**(ADF) and **11** are shown in Figure 17. Orbital $53a$ of **11** shows a bent Ti–Ti bond, the cause of the more acute angle at O in **11** (Table 1).

Ti₂Pn₂(μ-O)(CO). A possible intermediate in the decomposition of $\text{Ti}_2\text{Pn}_2\text{CO}_2$, undetected as yet experimentally, is $\text{Ti}_2\text{Pn}_2(\mu\text{-O})\text{CO}$, in which a CO bond has broken, the detached O bridges the two Ti atoms, and the CO ligand formed is bonded to one of the Ti atoms. Geometry optimization gave a local minimum for such a species, structure **12**. The Ti–Ti distance (2.46 Å, 2.43 Å) is still indicative of Ti–Ti bonding but longer than found for **9**. The bridging O is placed asymmetrically, further from the Ti to which the CO is coordinated.

The HOMO of **12** (Figure 18) forms a Ti–Ti bond but also has a role in back-bonding to the CO. The CO stretching vibration has a high wavenumber (1954 cm⁻¹, 1945 cm⁻¹), consistent with the small amount of back-bonding indicated by the HOMO. Binding of the bridging oxo ligand is spread over several MOs and has both σ and π character. The π bonding of O competes with the pentalene binding, resulting in an increase in the Ti–Pn ring C distances (Table 1).

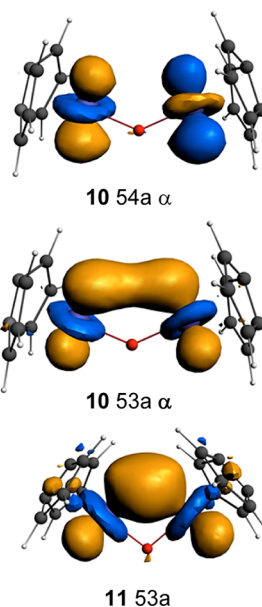


Figure 17. Metal-based orbitals of PnTiOTiPn in the triplet (**10**) and singlet (**11**) states.

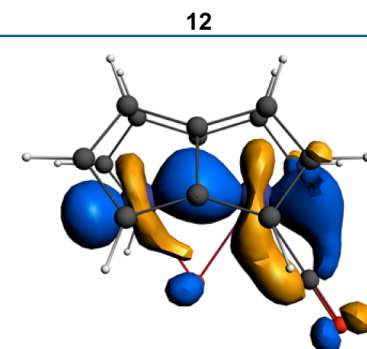
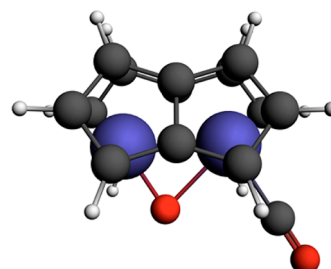


Figure 18. HOMO of $\text{Ti}_2\text{Pn}_2\text{O}(\text{CO})$ (**12**).

The energies of **3** and **12** are very close; ADF calculates **12** to be 1 kcal mol⁻¹ less stable than **3**, whereas Gaussian predicts **12** to be 11 kcal mol⁻¹ more stable than **3**.

Ti₂Pn₂S. The monosulfide derivative $\text{Ti}_2\text{Pn}_2^{\dagger}\text{S}$ can be synthesized by the reaction of $\text{Ti}_2\text{Pn}_2^{\dagger}$ with Ph_3PS .¹⁷ Geometry optimization of $\text{Ti}_2\text{Pn}_2\text{S}$ (**13**) gave a structure with dimensions in good agreement with the X-ray structure of $\text{Ti}_2\text{Pn}_2^{\dagger}\text{S}$.¹⁷

The Ti–Ti distance in **13** is longer than that calculated for the oxo analogue **9** but indicates Ti–Ti bonding. The HOMO of **13**, $13b_1$, is largely localized on the S and lies close in energy to the Ti–Ti bonding orbital $17a_1$ (Figure 19). Separation of the bonding interactions by symmetry shows a different pattern from the oxo analogue in that the b_2 interaction is the strongest and the a_1 interaction the weakest, although all three S 3p

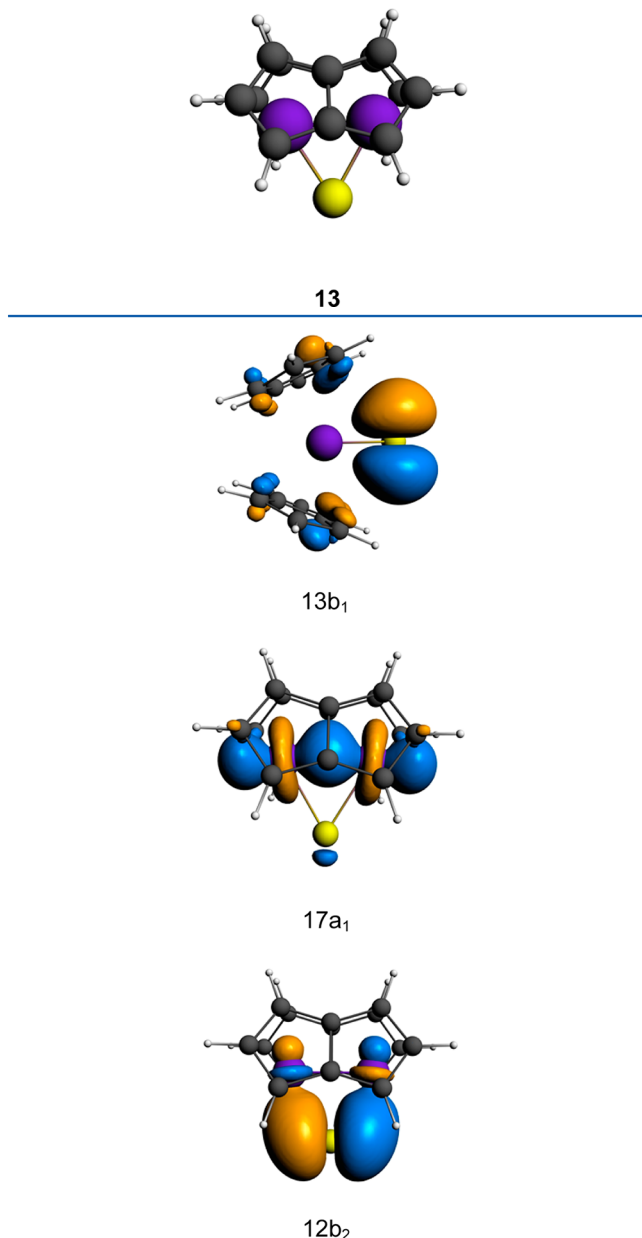


Figure 19. Selected orbitals for $\text{Ti}_2\text{Pn}_2\text{S}$, **13**.

orbitals contribute significantly to the bonding (Table 3). The Ti_2Pn_2 fragment occupancies (Table 4) also indicate less donation from the Ti atoms to the S than is found for O.

Ti₂Pn₂S(CO). There is good NMR evidence that $\text{Ti}_2\text{Pn}_2\text{S}$ binds CO reversibly.¹⁷ Geometry optimization of $\text{Ti}_2\text{Pn}_2\text{S}(\text{CO})$ (**14**) gives a similar structure to **12**. Binding of CO utilizes the Ti–Ti bonding orbital of **13**, as found for **12** and shown in Figure 20.

The Ti–Ti distance calculated for **14** is slightly longer than for **12** (Table 1) and the calculated CO stretch slightly lower (Table 6), both comparisons suggesting that donation from the Ti–Ti bonding orbital is greater for **14**, consistent with the lower electronegativity of S compared with O. The CO ligand has a rather low free energy of binding (Table 5), consistent with rapid exchange in solution, as evidenced by the NMR spectrum.¹⁷

The relative energies calculated for **14** and **5** differ from the oxo analogues; both methods predict **14** to be more stable

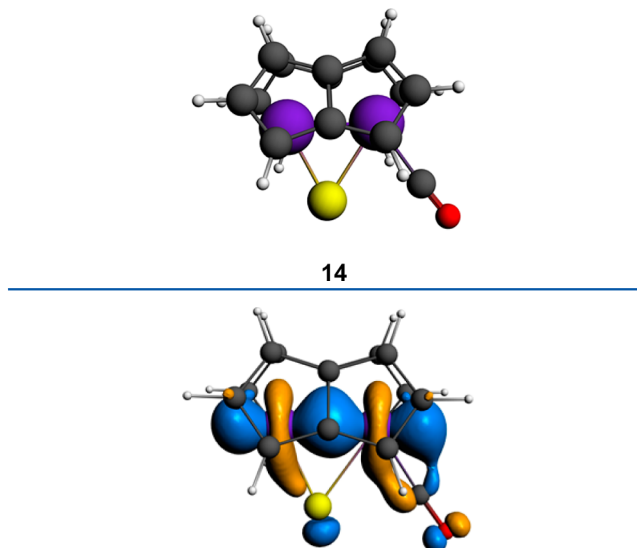
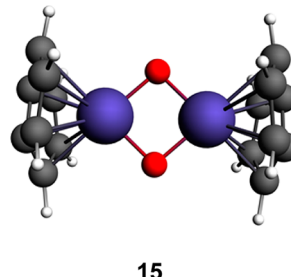


Figure 20. Isosurface of the $34a'$ orbital of **14** showing back-donation to CO from the Ti–Ti bonding orbital.

(ADF (BP/TZP) by 14 kcal mol⁻¹, Gaussian (B3LYP/SDD) by 9 kcal mol⁻¹).

PnTi(O)₂TiPn. $\text{Pn}^{\dagger}\text{Ti}(\mu\text{-O})_2\text{TiPn}^{\dagger}$ is one of the products obtained from the reductive disproportionation of CO_2 by $\text{Ti}_2\text{Pn}^{\dagger}_2$, and structural parameters of the optimized structure of $\text{PnTi}(\mu\text{-O})_2\text{TiPn}$ (**15**) (Table 1) are in good agreement with



15

those obtained experimentally.¹⁷ There is no Ti–Ti bonding, as the Ti atoms are in the IV oxidation state; the Ti–Ti distance of 2.74 Å (Table 1) is constrained by the short bonds to the bridging O atoms. The HOMO and HOMO–1 (Figure 21) represent δ bonds binding the pentalene ligands.

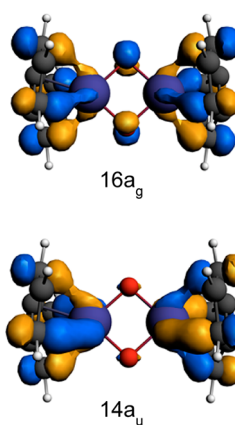


Figure 21. HOMO and HOMO–1 of $\text{PnTiO}_2\text{TiPn}$.

CONCLUSIONS

Ti_2Pn_2 has three frontier orbitals, two occupied high-lying metal–metal bonding orbitals and one low-lying LUMO, which enable this particular complex to display a range of reactivities not found with other double-sandwich compounds of this class. Its electron-rich nature dominates the chemistry, and it acts as a donor to CO_2 , CS_2 , and COS and is able to bind one, two, or three CO groups. The three frontier orbitals are of a_1 symmetry, and as a consequence, a single CO molecule binds in a sideways manner. Complexes may be formed with O and S, which maintain the sandwich structure, and in these cases the chalcogen atoms compete effectively with the pentalene ligands for the Ti d orbitals and form strong interactions of a_1 , b_1 , and b_2 symmetry involving all three chalcogen p orbitals. All of the compounds that maintain the double-sandwich structure of Ti_2Pn_2 maintain significant Ti–Ti bonding character.

EXPERIMENTAL SECTION

Computational Methods. Density functional theory calculations were carried out using two methods. One method employed the Amsterdam Density Functional package (version ADF2012.01).³⁷ The Slater-type orbital (STO) basis sets were of triple- ζ quality augmented with one polarization function (ADF basis TZP). Core electrons were frozen (C 1s; S and Ti 2p) in our model of the electronic configuration for each atom. The local density approximation (LDA) by Vosko, Wilk, and Nusair (VWN)³⁸ was used together with the exchange–correlation corrections of Becke and Perdew (BP86).^{39–41} The other method used Gaussian 09, revision A.02,⁴² with the B3LYP functional and SDD basis set. In both sets of calculations, tight optimization conditions were used, and frequency calculations were used to confirm stationary points. With the ADF code, molecules were subjected to fragment analyses in which the MOs of fragments, with the same geometries as they possess in the molecules, were used as the basis set for a full molecular calculation.

General Synthetic Procedures. All manipulations were carried out using standard Schlenk techniques under Ar or in an MBraun glovebox under N_2 or Ar. All glassware was dried at 160 °C overnight prior to use. Solvents were purified by predrying over sodium wire and then distilled over Na (toluene), K (methylcyclohexane), or Na–K alloy (Et_2O , hexane, and pentane) under a N_2 atmosphere. Dried solvents were collected, degassed, and stored over argon in K-mirrored ampules. Deuterated solvents were degassed by three freeze–pump–thaw cycles, dried by refluxing over K for 3 days, vacuum-distilled into ampules, and stored under N_2 . The gases used were of very high purity; CO (99.999%) and isotopically enriched ^{13}CO (99.7%) were supplied by Union Carbide and Euriso-top, respectively, and were added via Toepler pump. The compound $Ti_2Pn_2^+$ was prepared according to published procedures.¹⁴ NMR spectra were recorded on a Varian VNMRS 400 spectrometer (1H , 399.5 MHz; $^{13}C\{^1H\}$, 100.25 MHz; $^{29}Si\{^1H\}$, 79.4 MHz). The 1H and ^{13}C spectra were referenced internally to the residual protic solvent (1H) or the signals of the solvent (^{13}C). $^{29}Si\{^1H\}$ NMR spectra were referenced externally relative to $SiMe_4$. IR spectra were recorded between NaCl plates using a PerkinElmer Spectrum One FTIR instrument or a Mettler-Toledo ReactIR system featuring an IR probe inside a gas-tight cell attached to a Toepler pump. Continuous-wave EPR spectroscopy was carried out by Dr. W. K. Meyers from the CÆSR Facility at the University of Oxford using an X-band Bruker EMXmicro spectrometer. Simulations were made with the Win-EPR suite. Mass spectra were recorded using a VG Autospec Fisons instrument (EI at 70 eV). Elemental analyses were carried out by S. Boyer at the Elemental Analysis Service, London Metropolitan University. Solid-state magnetic measurements were carried out by A.-C. Schmidt at FAU Erlangen using a Quantum Design MPMS-5 SQUID magnetometer. Accurately weighed samples (ca. 20 mg) were placed into gelatin capsules and then loaded into nonmagnetic plastic straws before being lowered into the cryostat. Samples used for magnetization measurements were recrystallized

multiple times and checked for chemical composition and purity by elemental analysis and EPR spectroscopy. Values of the magnetic susceptibility were corrected for the underlying diamagnetic increment using tabulated Pascal constants⁴³ and the effect of the blank sample holders (gelatin capsule/straw).

Synthesis of $[Ti_2(\mu:\eta^5,\eta^5-Pn^+)_2][B(C_6F_5)_4]$. To a stirred, solid mixture of $Ti_2Pn_2^+$ (132 mg, 0.143 mmol) and $[FeCp^*_2][B(C_6F_5)_4]$ (143 mg, 0.142 mmol) at –35 °C was added Et_2O (20 mL), precooled to –78 °C, and the resultant brown mixture was allowed to warm to room temperature. After 12 h, the solvent was removed under reduced pressure to afford a brown residue that was washed thoroughly with pentane (4 × 20 mL) to remove $FeCp^*_2$ until the washings ran colorless. The residue was then extracted with Et_2O (2 × 10 mL) and concentrated to ca. 5 mL, and 5 drops of hexane were added. Cooling this solution to –35 °C produced brown-green crystals, which were isolated by decantation and dried in vacuo. Total yield: 125 mg (55% with respect to $Ti_2Pn_2^+$). ^{19}F NMR ($THF-d_8$, 375.9 MHz, 303 K): δ_F –132.7 (br, o-F), –165.2 (t, $^3J_{FF}$ = 20.2 Hz, p-F), –168.7 (br t, $^3J_{FF}$ = 19.3 Hz, m-F). $^{11}B\{^1H\}$ NMR ($THF-d_8$, 128.2 MHz, 303 K): δ_B –14.75. EPR (solid state, 293 K, X-band): g_1 = 2.003, g_2 = g_3 = 1.944, g_{iso} = 1.964. EI-MS: no volatility. Anal. Found (Calcd for $C_{76}H_{92}BF_{20}Si_4Ti_2$): C, 56.72 (56.89); H, 5.83 (5.78) %. Magnetic susceptibility: (Evans method, $THF-d_8$, 303 K) μ_{eff} = 1.96 μ_B per dimer; (SQUID, 260 K) μ_{eff} = 1.92 μ_B per dimer. Crystal data for $[Ti_2(\mu:\eta^5,\eta^5-Pn^+)_2][B(C_6F_5)_4] \cdot \frac{1}{2}(C_6H_{14})$: $C_{79}H_{99}BF_{20}Si_4Ti_2$, M_r = 1647.55, triclinic, space group $\overline{P}\bar{1}$, green plates, a = 14.217(3) Å, b = 15.491(3) Å, c = 19.366(4) Å, α = 89.30(3)°, β = 88.71(3)°, γ = 67.67(3)°, V = 3944.1(16) Å³, T = 100 K, Z = 2, R_{int} = 0.079, $\lambda_{Mo\text{Ka}}$ = 0.71075 Å, θ_{max} = 26.372°, R_1 [$I > 2\sigma(I)$] = 0.0562, wR_2 (all data) = 0.1656, GOF = 1.025.

Synthesis of $(\mu:\eta^5,\eta^5-Pn^+)_2Ti_2(CO)_3$. To a degassed solution of $Ti_2Pn_2^+(CO)_2$ (10 mg, 0.0108 mmol) in methylcyclohexane- d_{14} (0.5 mL) at –78 °C was added ^{13}CO (0.85 bar). Warming of the mixture resulted in a color change from green-brown to orange-brown. NMR yield: quantitative with respect to $Ti_2Pn_2^+(CO)_2$. 1H NMR (methylcyclohexane- d_{14} , 399.5 MHz, 303 K): δ_H 7.31 (2H, d, $^3J_{HH}$ = 2.9 Hz, Pn H), 7.22 (2H, br s, $\Delta\nu_{1/2}$ = 10 Hz, Pn H), 5.10 (2H, d, $^3J_{HH}$ = 2.8 Hz, Pn H), 4.96 (2H, d, $^3J_{HH}$ = 3.0 Hz, Pn H), 1.59 (6H, m, 1Pr CH), 1.43 (6H, m, 1Pr CH), 1.20 (18H, d, $^3J_{HH}$ = 7.4 Hz, 1Pr CH₃), 1.17 (18H, d, $^3J_{HH}$ = 7.4 Hz, 1Pr CH₃), 1.08 (18H, d, $^3J_{HH}$ = 7.4 Hz, 1Pr CH₃), 0.93 (18H, d, $^3J_{HH}$ = 7.4 Hz, 1Pr CH₃). 1H NMR (methylcyclohexane- d_{14} , 399.5 MHz, 193 K): δ_H 7.00 (2H, s, Pn H), 6.00 (2H, s, Pn H), 5.47 (2H, s, Pn H), 5.29 (2H, s, Pn H), 1.60 (6H, s, 1Pr CH), 1.44 (6H, s, 1Pr CH), 1.26–1.08 (36H, overlapping m, 1Pr CH₃), 1.02 (18H, s, 1Pr CH₃), 0.84 (18H, s, 1Pr CH₃). $^{13}C\{^1H\}$ NMR (methylcyclohexane- d_{14} , 100.5 MHz, 303 K): δ_C 232.1 (br, $\Delta\nu_{1/2}$ = 190 Hz, CO), 128.3 (Pn C), 123.3 (Pn C), 123.0 (Pn C), 122.8 (Pn C), 106.3 (Pn C), 103.9 (Pn C), 91.3 (Pn C), 86.2 (Pn C), 21.0 (1Pr CH₃), 20.9 (1Pr CH₃), 20.8 (1Pr CH₃), 20.4 (1Pr CH₃), 15.3 (1Pr CH), 13.9 (1Pr CH). $^{13}C\{^1H\}$ NMR (methylcyclohexane- d_{14} , 100.5 MHz, 193 K): δ_C 267.8 (CO), 256.7 (CO), 185.9 (free CO), 128.6 (Pn C), 119.0 (Pn C), 115.1 (Pn C), 114.5 (Pn C), 100.3 (Pn C), 96.2 (Pn C), 91.6 (Pn C), 90.5 (Pn C), 21.2 (1Pr CH₃), 21.0 (1Pr CH₃), 20.9 (1Pr CH₃), 15.4 (1Pr CH), 13.5 (1Pr CH). $^{29}Si\{^1H\}$ NMR (methylcyclohexane- d_{14} , 79.4 MHz, 303 K): δ_{Si} 3.59, 3.09. IR (methylcyclohexane, –65 °C): $Ti_2Pn_2^{+}(^{12}CO)_2$ 1991 (w, ν_{CO}), 1910 (s, ν_{CO}); $Ti_2Pn_2^{+}(^{13}CO)_2$ 1948 (w, $\nu_{^{13}CO}$), 1867 (s, $\nu_{^{13}CO}$) cm^{–1}. EI-MS: m/z 923 (100%) [M – 3CO]⁺. Anal. Found (Calcd for $C_{55}H_{92}O_3Si_4Ti_2$): C, 65.53 (65.44); H, 9.27 (9.19) %.

Crystallographic Details. Single-crystal XRD data for $[Ti_2(\mu:\eta^5,\eta^5-Pn^+)_2][B(C_6F_5)_4]$ were collected by the U.K. National Crystallography Service (NCS),⁴⁴ at the University of Southampton on a Rigaku FR-E + Ultra High Flux diffractometer ($\lambda_{Mo\text{Ka}}$) equipped with VariMax VHF optics and a Saturn 724+ CCD area detector. The data were collected at 150 K using an Oxford Cryosystems Cobra low-temperature device. Data collected by the NCS were processed using CrystalClear-SM Expert 3.1 b18,⁴⁵ and the unit cell parameters were refined against all data. Data were processed using CrysAlisPro (version 1.171.36.32),⁴⁶ and the unit cell parameters were refined

against all data. An empirical absorption correction was carried out using the Multi-Scan program.⁴⁷ The structure was solved using SHELXL-2013⁴⁸ and refined on F_o^2 by full-matrix least-squares refinements using SHELXL-2013.⁴⁸ Solutions and refinements were performed using the OLEX2⁴⁹ or WinGX⁵⁰ package and software packages within. All non-hydrogen atoms were refined with anisotropic displacement parameters. All hydrogen atoms were refined using a riding model.

■ ASSOCIATED CONTENT

Supporting Information

Detailed X-ray, IR, EPR, NMR, and CV data; a text file of computed molecule Cartesian coordinates for all structures in xyz format for convenient visualization; crystallographic data for $[\text{Ti}_2(\mu:\eta^5,\eta^5-\text{Pn}^\dagger)]_2[\text{B}(\text{C}_6\text{F}_5)_4]$ in CIF format. The Supporting Information is available free of charge on the ACS Publications website at DOI: 10.1021/acs.organomet.5b00363.

■ AUTHOR INFORMATION

Corresponding Authors

*E-mail for F.G.N.C.: f.g.cloke@sussex.ac.uk.

*E-mail for J.C.G.: jennifer.green@chem.ox.ac.uk.

Notes

The authors declare no competing financial interest.

■ ACKNOWLEDGMENTS

We thank the European Research Council and the University of Sussex for financial support. A.-C. Schmidt (SQUID magnetometry), Dr. W. K. Meyers (EPR spectroscopy), Dr. I. J. Day (NMR spectroscopy), and Dr. P. N. Horton (X-ray crystallography) are also acknowledged.

■ REFERENCES

- (1) Summerscales, O. T.; Cloke, F. G. N. *Coord. Chem. Rev.* **2006**, *250*, 1122–1140.
- (2) Green, M. L. H. *J. Organomet. Chem.* **1995**, *500*, 127–148.
- (3) Parkin, G. In *Comprehensive Organometallic Chemistry III*; Crabtree, R. H., Mingos, D. M. P., Eds.; Elsevier: Oxford, U.K., 2006; Vol. 1, pp 1–57.
- (4) www.covalentbondclass.org (accessed June 5, 2015).
- (5) Cloke, F. G. N.; Green, J. C.; Jardine, C. N. *Organometallics* **1999**, *18*, 1087–1090.
- (6) Cloke, F. G. N.; Green, J. C.; Kaltsoyannis, N. *Organometallics* **2004**, *23*, 832–835.
- (7) Balazs, G.; Cloke, F. G. N.; Gagliardi, L.; Green, J. C.; Harrison, A.; Hitchcock, P. B.; Shahi, A. R. M.; Summerscales, O. T. *Organometallics* **2008**, *27*, 2013–2020.
- (8) Katz, T. J.; Acton, N. *J. Am. Chem. Soc.* **1972**, *94*, 3281–3283.
- (9) Katz, T. J.; Acton, N.; McGinnis, J. *J. Am. Chem. Soc.* **1972**, *94*, 6205–6206.
- (10) Kuchta, M.; Cloke, F. G. N. *Organometallics* **1998**, *17*, 1934–1936.
- (11) Balazs, G.; Cloke, F. G. N.; Harrison, A.; Hitchcock, P. B.; Green, J.; Summerscales, O. T. *Chem. Commun.* **2007**, 873–875.
- (12) Ashley, A. E.; Cooper, R. T.; Wildgoose, G. G.; Green, J. C.; O'Hare, D. *J. Am. Chem. Soc.* **2008**, *130*, 15662–15677.
- (13) Summerscales, O. T.; Rivers, C. J.; Taylor, M. J.; Hitchcock, P. B.; Green, J. C.; Cloke, F. G. N. *Organometallics* **2012**, *31*, 8613–8617.
- (14) Kilpatrick, A. F. R.; Green, J. C.; Cloke, F. G. N.; Tsoureas, N. *Chem. Commun.* **2013**, *49*, 9434–9436.
- (15) Green, J. C.; Green, M. L. H.; Parkin, G. *Chem. Commun.* **2012**, *48*, 11481–11503.
- (16) Kilpatrick, A. F. R.; Cloke, F. G. N. *Chem. Commun.* **2014**, *50*, 2769–2771.
- (17) Kilpatrick, A. F. R.; Green, J. C.; Cloke, F. G. N. *Organometallics* **2015**, DOI: 10.1021/acs.organomet.5b00315.
- (18) Bendjaballah, S.; Kahlal, S.; Costuas, K.; Bévilhon, E.; Saillard, J.-Y. *Chem.—Eur. J.* **2006**, *12*, 2048–2065.
- (19) Lauher, J. W.; Hoffmann, R. *J. Am. Chem. Soc.* **1976**, *98*, 1729–1742.
- (20) Brintzinger, H. H.; Bartell, L. S. *J. Am. Chem. Soc.* **1970**, *92*, 1105–1107.
- (21) Brintzinger, H. H.; Lohr, L. L.; Wong, K. L. T. *J. Am. Chem. Soc.* **1975**, *97*, 5146–5155.
- (22) Petersen, J. L.; Dahl, L. F. *J. Am. Chem. Soc.* **1975**, *97*, 6416–6422.
- (23) Fieselmann, B. F.; Hendrickson, D. N.; Stucky, G. D. *Inorg. Chem.* **1978**, *17*, 2078–2084.
- (24) Albright, T. A.; Burdett, J. K.; Whangbo, M.-H. *Orbital Interactions in Chemistry*, 2nd ed.; John Wiley & Sons: Hoboken, NJ, 2013.
- (25) Green, J. C. *Chem. Soc. Rev.* **1998**, *27*, 263–271.
- (26) Compton, R. G.; Banks, C. E. *Understanding Voltammetry*, 2nd ed.; Imperial College Press: London, 2011.
- (27) Hanna, T. E.; Lobkovsky, E.; Chirik, P. J. *Organometallics* **2009**, *28*, 4079–4088.
- (28) Gericke, H. J.; Barnard, N. I.; Erasmus, E.; Swarts, J. C.; Cook, M. J.; Aquino, M. A. S. *Inorg. Chim. Acta* **2010**, *363*, 2222–2232.
- (29) Geiger, W. E.; Barrière, F. *Acc. Chem. Res.* **2010**, *43*, 1030–1039.
- (30) Bouwkamp, M. W.; de Wolf, J.; Del Hierro Morales, I.; Gercama, J.; Meetsma, A.; Troyanov, S. I.; Hessen, B.; Teuben, J. H. *J. Am. Chem. Soc.* **2002**, *124*, 12956–12957.
- (31) Hitchcock, P. B.; Kerton, F. M.; Lawless, G. A. *J. Am. Chem. Soc.* **1998**, *120*, 10264–10265.
- (32) Horáček, M.; Kupfer, V.; Thewalt, U.; Štěpníčka, P.; Polášek, M.; Mach, K. *Organometallics* **1999**, *18*, 3572–3578.
- (33) Evans, J. *J. Chem. Soc.* **1959**, 2003–2005.
- (34) Schubert, E. M. *J. Chem. Educ.* **1992**, *69*, 62.
- (35) Cordero, B.; Gomez, V.; Platero-Prats, A. E.; Reves, M.; Echeverria, J.; Cremades, E.; Barragan, F.; Álvarez, S. *Dalton Trans.* **2008**, 2832–2838.
- (36) Brisdon, A. K. *Inorganic Spectroscopic Methods*; Oxford Chemistry Primers, Vol. 62; Oxford University Press: Oxford, U.K., 1998.
- (37) *Amsterdam Density Functional (ADF) Modeling Suite*; Scientific Computing and Modelling NV: Amsterdam, 2006.
- (38) Vosko, S. H.; Wilk, L.; Nusair, M. *Can. J. Phys.* **1980**, *58*, 1200–1211.
- (39) Becke, A. *Phys. Rev., A* **1988**, *38*, 3098–3100.
- (40) Perdew, J. P. *Phys. Rev. B* **1986**, *33*, 8822–8824.
- (41) Perdew, J. P. *Phys. Rev. B* **1986**, *34*, 7406.
- (42) Frisch, M. J.; Trucks, G. W.; Schlegel, H. B.; Scuseria, G. E.; Robb, M. A.; Cheeseman, J. R.; Scalmani, G.; Barone, V.; Mennucci, B.; Petersson, G. A.; Nakatsuji, H.; Caricato, M.; Li, X.; Hratchian, H. P.; Izmaylov, A. F.; Bloino, J.; Zheng, G.; Sonnenberg, J. L.; Hada, M.; Ehara, M.; Toyota, K.; Fukuda, R.; Hasegawa, J.; Ishida, M.; Nakajima, T.; Honda, Y.; Kitao, O.; Nakai, H.; Vreven, T.; Montgomery, J. A., Jr.; Peralta, J. E.; Ogliaro, F.; Bearpark, M.; Heyd, J. J.; Brothers, E.; Kudin, K. N.; Staroverov, V. N.; Kobayashi, R.; Normand, J.; Raghavachari, K.; Rendell, A.; Burant, J. C.; Iyengar, S. S.; Tomasi, J.; Cossi, M.; Rega, N.; Millam, J. M.; Klene, M.; Knox, J. E.; Cross, J. B.; Bakken, V.; Adamo, C.; Jaramillo, J.; Gomperts, R.; Stratmann, R. E.; Yazeyev, O.; Austin, A. J.; Cammi, R.; Pomelli, C.; Ochterski, J. W.; Martin, R. L.; Morokuma, K.; Zakrzewski, V. G.; Voth, G. A.; Salvador, P.; Dannenberg, J. J.; Dapprich, S.; Daniels, A. D.; Farkas, Ö.; Foresman, J. B.; Ortiz, J. V.; Cioslowski, J.; Fox, D. J. *Gaussian 09*, revision A.02; Gaussian, Inc.: Wallingford, CT, 2009.
- (43) Bain, G. A.; Berry, J. F. *J. Chem. Educ.* **2008**, *85*, 532–536.
- (44) Coles, S. J.; Gale, P. A. *Chem. Sci.* **2012**, *3*, 683–689.
- (45) *CrystalClear*; Rigaku: Tokyo, 2011.
- (46) *CrysAlisPro*, version 1.171.36.32; Agilent Technologies: Santa Clara, CA, 2011.
- (47) Blessing, R. H. *Acta Crystallogr., Sect. A* **1995**, *51*, 33–38.
- (48) Sheldrick, G. M. *Acta Crystallogr., Sect. A* **2008**, *64*, 112–122.

- (49) Dolomanov, O. V.; Bourhis, L. J.; Gildea, R. J.; Howard, J. A. K.; Puschmann, H. *J. Appl. Crystallogr.* **2009**, *42*, 339–341.
(50) Farrugia, L. J. *J. Appl. Crystallogr.* **1999**, *32*, 837–838.